A STUDY OF P-BAND PENETRATION CAPABILITIES: APPLICATION IN SUB-SURFACE REMOTE SENSING

S. REDADAA[1], A. BOUALLEG[1], N. MERABTINE[2], M. BENSLAMA[2]

[1] Computer Science and Telecommunications Laboratory,
Guelma University, 24000, Guelma, Algeria
[2] Electromagnetism and Telecommunications Laboratory
Mentouri University, 25000, Constantine, Algeria
E-mail: salah.redadaa@enst-bretagne.fr, redasdz@yahoo.fr

Received January 15, 2007

Low-frequency active microwaves allow one to investigate the sub-surface down to several meters under some conditions. So far, few studies were conducted in this field. This paper addresses the problem of attenuation due to the sub-surface propagation phenomenon. The theoretical study about soil propagation predicts attenuation which strongly depends on incidence angle, on polarization, and most of all, on moist content. The simulation of the attenuation was done for various soil types for different polarizations. In P-band (435 MHz), we have obtained a penetration depth up to 17 meters for a dry soil before 3 dB attenuation of the incident wave.

Key words: low-frequency, sub-surface, wave propagation, soil moisture.

1. INTRODUCTION

Active microwaves sensors include radar imagers, scatterometters and altimeters [1]. Low-frequency radar imagers allow us to investigate the sub-surface down to several meters over arid areas, when covered by dry material such as sand [2–6]. Sub-surface imaging presents then high potential for terrestrial applications in arid and semi-arid environments, such as hydrology, geological mapping, natural hazard monitoring, and archaeology. Sub-surface geology down to a couple of meters is made of a complex combination of materials (generally sediments) and structures, and the ground truth needed for model development and inversion is hard to obtain. Few outdoor and laboratory experiments were conducted to actually measure the microwave penetration in desert soils [4, 7–11], and approaches based on a combination of GPR (Ground Penetrating Radar) and active microwave data proved to be successful: the GPR is operated to derive geometrical and dielectric characteristics of the sub-surface structures which are then used as input for the interpretation of the radar image [12, 9].

One of the most intersting results regarding sub-surface imaging obtained with active microwaves was obtained more than 20 years ago by McCauley *et al.*, [2] for a site located in southern Egypt, the Bir Safsaf region, using the Shuttle Imaging Radar (SIR). SIR-A radar revealed buried and previously unknown paleodrainage channels. Severals field expeditions were afterwards undertaken in this region in order to explore and understand the geology of sub-surface structures and their relationship with the radar signal [4, 6, 9]. However, the limited geographical coverage of Shuttle Imaging Radar missions did not allow regional scale mapping of hidden hydrological and tectonic structures of East Sahara, and scientific interpretations of available data remain partial and incomplete.

This paper is organized as follows. Section 2 introduces the formulation of reflection and transmission of electromagnetic waves for one-layer and layered media. Section 3 presents the Schwarz-Wang soil permittivity model. Section 4 is devoted to the simulation of the P-band sub-surface wave propagation and finally a conclusion is given.

2. REFLECTION AND TRANSMISSION OF ELECTROMAGNETIC WAVES

2.1. REFLECTION AND TRANSMISSION OF TE WAVES

For the TE (transverse electric) plane wave incident on the isotropic medium, the total electric and magnetic fields in region 0 are the sum of the reflected and incident components Fig. 1, [1, 13–14]. We write

$$E_y = (RE_0 e^{ik_z z} + E_0 e^{-ik_z z}) e^{ik_x x} \tag{1}$$

$$H_x = -\frac{k_z}{\omega \mu_0} (RE_0 e^{ik_z z} - E_0 e^{-ik_z z}) e^{ik_x x} \tag{2}$$

$$H_z = \frac{k_x}{\omega \mu_0} (RE_0 e^{ik_z z} + E_0 e^{-ik_z z}) e^{ik_x x} \tag{3}$$

where E_0 is the incident wave amplitude and R denotes the reflection coefficient for electric fields. In the exponents of (1)–(3), the x components of wavenumber vector for the incident and reflected waves are equal by virtue of phase matching. The z components are opposite in sign, indicating that the reflected and incident waves are propagating along the opposite $\hat{z}$ directions. The magnitude are equal because they obey the same dispersion relation

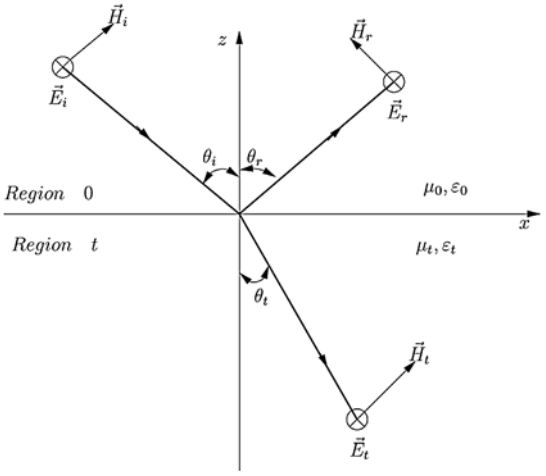

Fig. 1 – Reflection and transmission of TE waves at a plane boundary.

$$k_x^2 + k_z^2 = \omega^2 \mu_0 \varepsilon_0 \tag{4}$$

In region *t*, there is only a transmitted wave. The TE wave solutions take the form

$$E_{ty} = TE_0 e^{-ik_{tz}z + ik_x x} \tag{5}$$

$$H_{tx} = -\frac{k_{tz}}{\omega \mu_t} TE_0 e^{-ik_{tz}z + ik_x x} \tag{6}$$

$$H_{tz} = \frac{k_x}{\omega \mu_t} TE_0 e^{-ik_{tz}z + ik_x x} \tag{7}$$

where T denotes the transmission coefficient for the electric field. Again this set of equations satisfies Maxwell's equations and the dispersion relation

$$k_x^2 + k_{tz}^2 = \omega^2 \mu_t \varepsilon_t \tag{8}$$

The x component of $\vec{k}_t$ is equal to those of the incident and reflected waves on account of phase matching.

If we consider that the boundary surface at $z = 0$ where the tangential components of $\vec{E}$ and $\vec{H}$ are continuous. Then, we obtain

$$1 + R = T \tag{9}$$

$$\frac{k_z}{\mu_0}(1 - R) = \frac{k_{tz}}{\mu_t} T \tag{10}$$

The reflection and transmission coefficients R and T are easily determined from (9) and (10),

$$R = R_{0t} = \frac{1 - p_{0t}}{1 + p_{0t}} \tag{11}$$

and

$$T = T_{0t} = \frac{2}{1 + p_{0t}} \tag{12}$$

where, for TE waves

$$p_{0t} = \frac{\mu_0 k_{tz}}{\mu_t k_z} \tag{13}$$

With p_{0t} for TE waves defined in (13), R_{0t} in (11) is the Fresnel reflection coefficient for a TE wave incident from region 0 and reflected at the boundary separating regions 0 and t. In (12) T_{0t} is the transmission coefficient from region 0 to region t.

We note that when the boundary surface is not at $z = 0$ but at $z = -d_0$, then the phases of the reflected and transmitted waves are dependent on the location of the boundary surface. The reflection coefficient gains a phase shift of $2k_z d_0$ and the transmission coefficient gains a phase shift of $(k_z - k_{tz})d_0$.

2.2. REFLECTION AND TRANSMISSION OF TM WAVES

The reflection and transmission of TM (transverse magnetic) waves by a plane boundary can be carried out in a manner similar to the treatment of the TE waves. We can also invoke the principle of duality and write down the answers directly. Making the replacement $\vec{E} \to \vec{H}$, , $\vec{H} \to -\vec{E}$, $\mu \rightleftharpoons \varepsilon$ and the boundary conditions of continuous tangential $\vec{H}$ and $\vec{E}$ at $z = 0$, we find the dual of the TE problem to be precisely the TM problem. We obtain the reflection and transmission coefficients as in (11)–(12) with p_{0t} in (13) replaced by

$$p_{0t} = \frac{\varepsilon_0 k_{tz}}{\varepsilon_t k_z} \tag{14}$$

for TM waves.

The reflection and transmission coefficients for both TE and TM waves are functions of the constitutive parameters of the two media forming the interface. For a given set of constitutive parameters, the incidence angle which reduces the reflection coefficient to zero is known as the Brewster angle θ_B [13]. We discuss the Brewster angle for nonmagnetic media where $\mu_0 = \mu_t$ by setting $R_{0t} = 0$ or $p_{0t} = 1$. From (13), we find,

$$k_{tz} = k_z \tag{15}$$

for TE waves, and from (14),

$$\varepsilon_0 k_{lz} = \varepsilon_t k_z \tag{16}$$

for TM waves. In view of the fact that $k_{lz} = k_z$ only if both dielectrics have identical permittivities, we see that no Brewster angle can exist for the TE waves. For TM waves, (16) can be written as

$$k \cos\theta_t = k_t \cos\theta_B \tag{17}$$

where we use the fact that $\varepsilon_0/\varepsilon_t = k^2/k_t^2$ and that $k_z = k\cos\theta_B$. Also, by Snell's law,

$$k \sin\theta_B = k_t \sin\theta_t \tag{18}$$

Cancelling k and k_t from (17) and (18) we find $\sin 2\theta_B = \sin 2\theta_t$. The solution $\theta_B = \theta_t$ again implies identical media and is of no interest. In view of the fact that both θ_B and θ_t are larger than zero and less than $\pi/2$, we obtain as the other solution,

$$\theta_B + \theta_t = \frac{\pi}{2} \tag{19}$$

Since the reflected direction is perpendicular to the transmitted direction, the reflected wave vector is perpendicular to the transmitted wave vector. substituting (19) in (18), we obtain the Brewster angle

$$\theta_B = \tan^{-1}\frac{k_t}{k} = \tan^{-1}\sqrt{\frac{\varepsilon_t}{\varepsilon_0}} \tag{20}$$

2.3. REFLECTION AND TRANSMISSION BY A LAYERED MEDIUM

We consider a plane wave incident on a stratified isotropic medium with boundaries at $z = -d_0, -d_1, \ldots, -d_n$ (Fig. 2). The $(n+1)$th region is semi-infinite and is labeled t, $t = n + 1$. The permittivity and permeability in each region are denoted by ε_l and μ_l. The plane wave is incident from region 0 and has the plane of incidence parallel to $x - z$ plane. All field vectors are dependent on x and z only and independent of y. Since $\partial/\partial y = 0$, Maxwell's equations in any region l can be separated into TE and TM components governed by E_{ly} and H_{ly}.

For a TE plane wave $E_y = E_0 e^{-i(k_z z - k_x x)}$, incident on the stratified medium, the total field in region l can be written as

$$E_{ly} = (A_l e^{ik_{lz}z} + B_l e^{-ik_{lz}z}) e^{ik_x x} \tag{21}$$

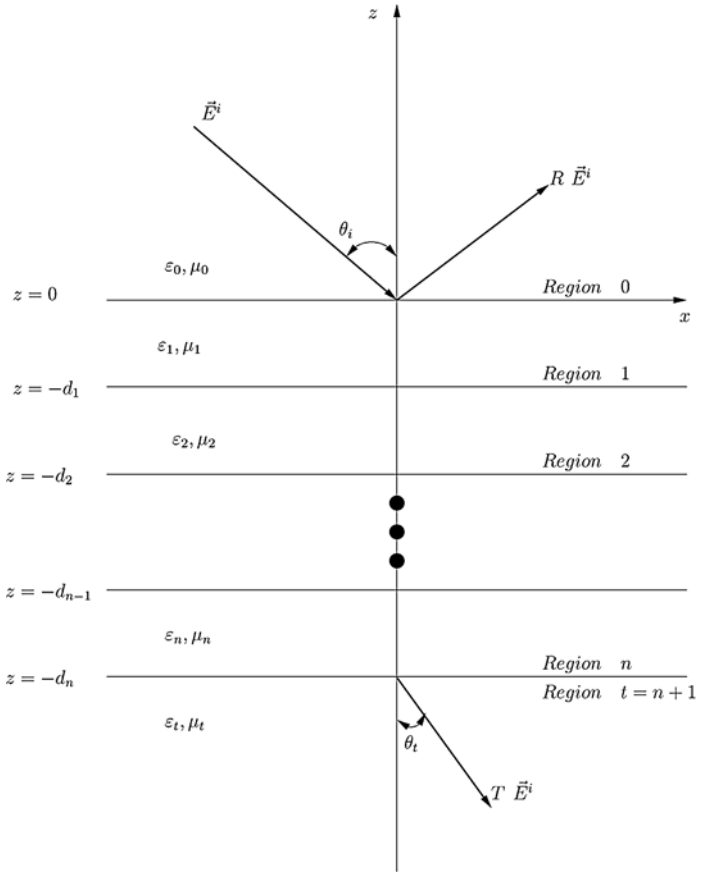

Fig. 2. Reflection and transmission for an *n*-layer medium.

$$H_{lx} = -\frac{k_{lz}}{\omega \mu_l}(A_l e^{ik_{lz}z} - B_l e^{-ik_{lz}z})e^{-ik_x x} \tag{22}$$

$$H_{lz} = \frac{k_x}{\omega \mu_l}(A_l e^{ik_{lz}z} + B_l e^{-ik_{lz}z})e^{ik_x x}. \tag{23}$$

In region 0 where $l = 0$, we obtain

$$A_0 = RE_0 \tag{24}$$

$$B_0 = E_0 \tag{25}$$

In region t where $l = n + 1 = t$, we have

$$A_t = 0 \tag{26}$$

$$B_t = TE_0 \tag{27}$$

The wave amplitudes A_l and B_l are related to wave amplitudes in neighboring region by the boundary conditions. At $z = -d_l$, boundary conditions require that E_y and H_x be continuous. We obtain

$$A_l e^{-ik_{lz}d_l} + B_l e^{ik_{lz}d_l} = A_{l+1} e^{-ik_{(l+1)z}d_l} + B_{l+1} e^{ik_{(l+1)z}d_l} \tag{28}$$

$$\frac{k_{lz}}{\mu_l}[A_l e^{-ik_{lz}d_l} - B_l e^{ik_{lz}d_l}] = \frac{k_{(l+1)z}}{\mu_{l+1}}[A_{l+1} e^{-ik_{(l+1)z}d_l} - B_{l+1} e^{ik_{(l+1)z}d_l}] \tag{29}$$

There are $(n + 1)$ boundaries which give rise to $2(n + 1)$ equations. In region 0, we have an unknown reflection coefficient R. In region t, we have an unknown transmission coefficient T. There are two unknowns A_l and B_l in each of the regions $l = 1, 2, \ldots, n$. Thus we have a total of $2(n + 1)$ unknowns from the $2(n + 1)$ linear equations, we can arrange the equations in matrix form with the unknowns forming a $(2n + 2)$ column matrix and the coefficients forming a $(2n + 2) \times (2n + 2)$ squarematrix. The solution is then obtained by inverting the square matrix. This procedure is straightforward but tedious. We shall now describe simpler ways to deals with the problem.

2.3.1. Reflection coefficients

Since we are interested in finding the reflection coefficient for the stratified medium, we research to derive a closed-form formula for R. We first solve (28) and (29) for A_l and B_l.

$$A_l e^{-ik_{lz}d_l} = \frac{1}{2}(1 + p_{l(l+1)})\left\{A_{l+1} e^{-ik_{(l+1)z}d_l} + R_{l(l+1)} B_{l+1} e^{ik_{(l+1)z}d_l}\right\} \tag{30}$$

$$B_l e^{ik_{lz}d_l} = \frac{1}{2}(1 + p_{l(l+1)})\left\{R_{l(l+1)} A_{l+1} e^{-ik_{(l+1)z}d_l} + B_{l+1} e^{ik_{(l+1)z}d_l}\right\} \tag{31}$$

where

$$p_{l(l+1)} = \frac{\mu_l k_{(l+1)z}}{\mu_{l+1} k_{lz}} \tag{32}$$

for the TE waves and

$$R_{l(l+1)} = \frac{1 - p_{l(l+1)}}{1 + p_{l(l+1)}} \tag{33}$$

is the reflection coefficient for waves in region l, caused by the boundary separating regions l and $l + 1$. We note from (32) that

$$p_{(l+1)l} = \frac{1}{p_{l(l+1)}} \tag{34}$$

which gives also

$$R_{(l+1)l} = -R_{l(l+1)} \tag{35}$$

Thus the reflection coefficient in region $l+1$, $R_{(l+1)l}$, caused by the boundary separating regions $l+1$ and l, is equal to the negative of $R_{l(l+1)}$.

Forming the ratio of (30) and (31) we obtain

$$\begin{aligned}\frac{A_l}{B_l} &= \frac{e^{i2k_{lz}d_l}}{R_{l(l+1)}} + \frac{[1-(1/R_{l(l+1)}^2)]e^{i2(k_{(l+1)z}+k_{lz})d_l}}{[1/R_{l(l+1)}]e^{i2k_{(l+1)z}d_l} + (A_{l+1}/B_{l+1})} = \\ &= \frac{e^{i2k_{lz}d_l}}{R_{l(l+1)}} + \frac{[1-(1/R_{l(l+1)}^2)]e^{i2(k_{(l+1)z}+k_{lz})d_l}\ |}{[1/R_{l(l+1)}]e^{i2k_{(l+1)z}d_l}} + \frac{A_{l+1}}{B_{l+1}}\end{aligned} \tag{36}$$

With the second equality we introduce a notation for writing a continued fraction. Equation (36) express A_l/B_l in terms of A_{l+1}/B_{l+1} and so on, until the transmitted region t, where $A_t/B_t = 0$, is reached.

The reflection coefficient due to the stratified medium is $R = A_0/B_0$. Making use of the continued fractions, we obtain

$$\begin{aligned}R = &\frac{e^{i2k_zd_0}}{R_{01}} + \frac{[1-(1/R_{01}^2)]e^{i2(k_{1z}+k_z)d_0}\ |}{(1/R_{01})e^{i2k_{1z}d_0}} + \frac{e^{i2k_{1z}d_1}}{R_{12}} + \\ &+ \frac{[1-(1/R_{12}^2)]e^{i2(k_{2z}+k_{1z})d_1}\ |}{(1/R_{12})e^{i2k_{2z}d_1}} + \cdots + \frac{e^{i2k_{(n-1)z}d_{n-1}}}{R_{(n-1)n}} + \\ &+ \frac{[1-(1/R_{(n-1)n}^2)]e^{i2(k_{nz}+k_{(n-1)z})d_{n-1}}\ |}{(1/R_{(n-1)n})e^{i2k_{nz}d_{n-1}}} + R_{nt}e^{i2k_{nz}d_n}\end{aligned} \tag{37}$$

This is a closed-form solution for the reflection coefficient expressed in continued fractions.

For the TM plane waves reflected from the stratified medium, the principle of duality applies and gives rise to the answer for R identical to (37). The only difference is that (32) now becomes

$$p_{l(l+1)} = \frac{\varepsilon_l k_{(l+1)z}}{\varepsilon_{l+1} k_{lz}} \tag{38}$$

for TM waves. Thus, for the definition of the reflection coefficients in (33), we shall use (38) instead of (32). For a two-layer medium, we find from (37), writting $k_{0z} = k_z$,

$$R = \frac{e^{i2k_zd_0}}{R_{01}} + \frac{[1-(1/R_{01}^2)]e^{i2(k_{1z}+k_z)d_0}}{(1/R_{01})e^{i2k_{1z}d_0} + R_{12}e^{i2k_{1z}d_1}} = \frac{R_{01} + R_{12}e^{i2k_{1z}(d_1-d_0)}}{1 + R_{01}R_{12}e^{i2k_{1z}(d_1-d_0)}}e^{i2k_zd_0} \tag{39}$$

2.3.2. Propagation matrices and transmission coefficients

For a plane wave incident on a stratified medium, we have obtained the boundary conditions of continuity of tangential electric and magnetic fields at each interface $z = -d_l$, with the two equations (28)–(29) relating wave amplitudes in regions l and $l + 1$:

$$A_{l+1}e^{-ik_{(l+1)z}d_l} + B_{l+1}e^{ik_{(l+1)z}d_l} = A_l e^{-ik_{lz}d_l} + B_l e^{ik_{lz}d_l} \tag{40}$$

$$A_{l+1}e^{-ik_{(l+1)z}d_l} - B_{l+1}e^{ik_{(l+1)z}d_l} = p_{(l+1)l}[A_l e^{-ik_{lz}d_l} - B_l e^{ik_{lz}d_l}] \tag{41}$$

In the last subsection we have determined the reflection coefficients $R = A_0/B_0$ from the $(2n + 2)$ boundary conditions. we will now show that the transmission coefficient $T = B_t/B_0$ can be obtained by the use of propagation matrices.

We solve for A_{l+1} and B_{l+1} in terms of A_l and B_l from (40)–(41) and obtain

$$\begin{aligned} A_{l+1}e^{-ik_{(l+1)z}d_{l+1}} &= \frac{1}{2}(1 + p_{(l+1)l})(A_l e^{-ik_{lz}d_l} + R_{(l+1)l}B_l e^{ik_{lz}d_l}) \\ B_{l+1}e^{ik_{(l+1)z}d_{l+1}} &= \frac{1}{2}(1 + p_{(l+1)l})(R_{(l+1)l}A_l e^{-ik_{lz}d_l} + B_l e^{ik_{lz}d_l}) \end{aligned} \tag{42}$$

Expressing in the form of matrix multiplication, we have

$$\begin{bmatrix} A_{l+1}e^{-ik_{(l+1)z}d_{l+1}} \\ B_{l+1}e^{ik_{(l+1)z}d_{l+1}} \end{bmatrix} = C_{(l+1)l} \cdot \begin{bmatrix} A_l e^{-ik_{lz}d_l} \\ B_l e^{ik_{lz}d_l} \end{bmatrix} \tag{43}$$

where

$$C_{(l+1)l} = \frac{1}{2}(1 + p_{(l+1)l}) \cdot \begin{bmatrix} e^{-ik_{(l+1)z}(d_{l+1}-d_l)} & R_{(l+1)l}e^{-ik_{(l+1)z}(d_{l+1}-d_l)} \\ R_{(l+1)l}e^{ik_{(l+1)z}(d_{l+1}-d_l)} & e^{ik_{(l+1)z}(d_{l+1}-d_l)} \end{bmatrix}, \tag{44}$$

is called the forward-propagating matrix. In (44), $R_{(l+1)l}$ is the reflection coefficient at the boundary separating $l + 1$ and l, and the the first subscript denotes the region with the incident wave. It is to be noted for the forward-propagating matrix between n and $t = n + 1$,

$$\begin{bmatrix} 0 \\ T \end{bmatrix} = C_{tn} \cdot \begin{bmatrix} A_n e^{-ik_{nz}d_n} \\ B_n e^{ik_{nz}d_n} \end{bmatrix} \tag{45}$$

with

$$C_{tn} = \frac{1}{2}(1 + p_{tn}) \cdot \begin{bmatrix} e^{ik_{tz}d_n} & R_{tn}e^{ik_{tz}d_n} \\ R_{tn}e^{-ik_{tz}d_n} & e^{-ik_{tz}d_n} \end{bmatrix} \tag{46}$$

By the same token, we may express A_l and B_l in terms of A_{l+1} and B_{l+1} by using (28)–(29) and define a backward-propagation matrix.

The propagation matrices can be used to determine waves amplitudes in any region in terms of those in any other region. For $m > l$, we make use of the forward propagation matrix to obtain

$$\begin{bmatrix} A_m e^{-ik_{mz}d_m} \\ B_m e^{ik_{mz}d_m} \end{bmatrix} = C_{m(m-1)} \cdot C_{(m-1)(m-2)} \ldots C_{(l+1)l} \cdot \begin{bmatrix} A_l e^{-ik_{lz}d_l} \\ B_l e^{ik_{lz}d_l} \end{bmatrix} \tag{47}$$

Similarly, backward-propagating matrices can be used to express wave amplitudes in any region j in terms of those in region l for $l > j$.

In paricular, the transmission coefficient $T = B_t/B_0$ for a stratified medium with $t = n + 1$ layers can be calculated by the multiplication of $n + 1$ propagation matrices. Using the forward-propagating matrices, we have

$$\begin{bmatrix} 0 \\ T \end{bmatrix} = C_{t0} \cdot \begin{bmatrix} Re^{-ik_z d_0} \\ e^{ik_z d_0} \end{bmatrix} \tag{48}$$

where

$$C_{t0} = C_{tn} \cdot C_{n(n-1)} \ldots C_{10} \tag{49}$$

includes all information about the stratified medium. Once C_{t0} is known, both the reflection and transmission coefficients can be calculated from its matrix elements.

As a first case, we calculate the transmission coefficient for a one-layer (half-space) medium. From (44) and by letting $d_0 = 0$, we find

$$\begin{bmatrix} 0 \\ T \end{bmatrix} = \frac{1}{2}(1 + p_{t0}) \begin{bmatrix} 1 & R_{t0} \\ R_{t0} & 1 \end{bmatrix} \begin{bmatrix} R_{0t} \\ 1 \end{bmatrix}, \tag{50}$$

which gives

$$T = \frac{1}{2}(1 + p_{t0})(1 - R_{0t}^2) = \frac{2}{1 + p_{0t}} \tag{51}$$

For a two-layer medium with $d_0 = 0$, we obtain the transmission coefficient from

$$\begin{aligned} \begin{bmatrix} 0 \\ T \end{bmatrix} = \frac{1}{4}(1 + p_{t1})(1 + p_{10}) &\begin{bmatrix} e^{ik_{tz}d_1} & R_{t1}e^{ik_{tz}d_1} \\ R_{t1}e^{-ik_{tz}d_1} & e^{-ik_{tz}d_1} \end{bmatrix} \times \\ \times &\begin{bmatrix} e^{-ik_{1z}d_1} & R_{10}e^{-ik_{1z}d_1} \\ R_{10}e^{ik_{1z}d_1} & e^{ik_{1z}d_1} \end{bmatrix} \begin{bmatrix} R \\ 1 \end{bmatrix}, \end{aligned} \tag{52}$$

which yields

$$T = \frac{1}{4}(1+p_{10})(1+p_{1t})\frac{(1-R_{01}^2)-(1-R_{1t}^2)}{1+R_{01}R_{1t}e^{i2k_{1z}d_1}}e^{i(k_{1z}-k_{tz})d_1} = \\ = \frac{4e^{i(k_{1z}-k_{tz})d_1}}{(1+p_{01})(1+p_{1t})(1+R_{01}R_{1t}e^{i2k_{1z}d_1})} \tag{53}$$

The above coefficients are for the electric fields. The power reflection coefficient or reflectivity Γ, and transmissivity ϒ are given by

$$\Gamma = |R|^2, \tag{54}$$

$$\Upsilon = p_{0t}\,|T|^2\,. \tag{55}$$

3. SCHWARZ–WANG SOIL PERMITTIVITY MODEL

Several dielectric models or mixing equations have been proposed for soil-water mixtures, including those of [15–18]. The mixing equation chosen for this work is due to that in [15] and is based on a dielectric relaxation theory. The Schwarz–Wang model was chosen in preference to the others because its gives both the real and the imaginary parts of the complex relative permittivity $\varepsilon(W, f)$ of soil-water mixtures as a function of frequency, *f*, and of the volumetric moisture content of the soil *W*. The parameters that it requires can be implemented in convenient form for numeric computation and it does not depend on parameters which may not be known in pratical situations, such as the soil temperature or composition [19–20].

The real and imaginary parts of the permittivity $\varepsilon(W, f) = \varepsilon'(W, f) - -i\varepsilon''(W, f)$ are specified as

$$\varepsilon'(W, f) = \varepsilon_\infty(W) + \frac{\varepsilon_s(W)-\varepsilon_\infty(W)}{2\beta(W)} \cdot \ln\left[\frac{e^{\beta(W)} + \left(\frac{f}{f_m(W)}\right)^2}{e^{-\beta(W)} + \left(\frac{f}{f_m(W)}\right)^2}\right] \tag{56}$$

and

$$\varepsilon''(W, f) = \frac{\varepsilon_s(W)-\varepsilon_\infty(W)}{\beta(W)} \cdot \tan^{-1}\left[\frac{(1-e^{-\beta(W)})\frac{f}{f_m(W)}}{e^{-\beta(W)/2}\left[1+\left(\frac{f}{f_m(W)}\right)^2\right]}\right] + \frac{\sigma(W)}{2\pi f \varepsilon_0} \tag{57}$$

where $\varepsilon_s(W)$ is the static (low frequency) relative permittivity

$$\varepsilon_s(W) = 3.14 + 23.83W + 91.58W^2 \tag{58}$$

and $\varepsilon_\infty(W)$ is the relative permittivity at high frequencies

$$\varepsilon_\infty(W) = \varepsilon_r(1-l) + \varepsilon_a(l-W) + 4W. \tag{59}$$

$l \approx 0.5$ is the porosity of the soil, $\varepsilon_a = 1$ is the dielectric constant of air, and $\varepsilon_r \approx 5$ is the dielectric constant of rock. The remaining parameters – the

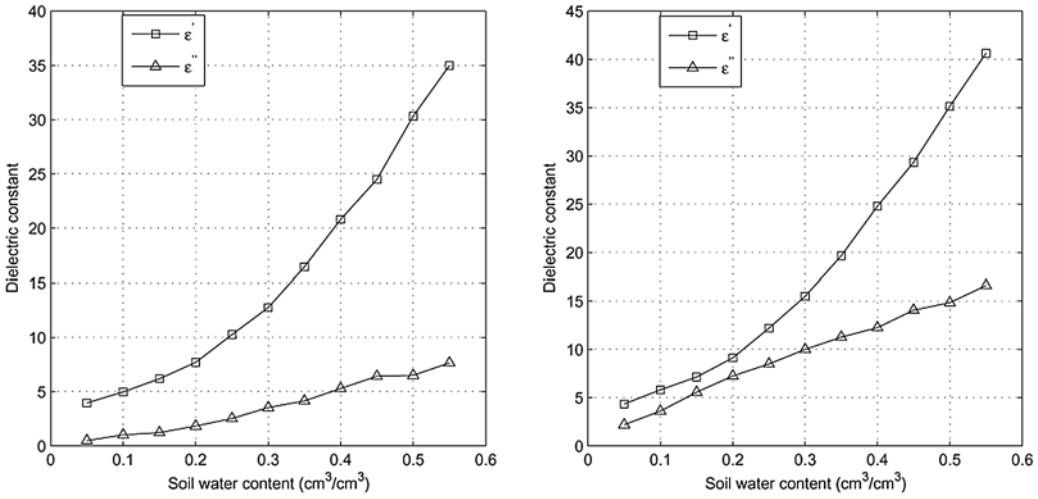

(a) L-band (b) P-band

Fig. 3 – Dielectric constants of a high clay content soil as function of water content for L- and P- bands.

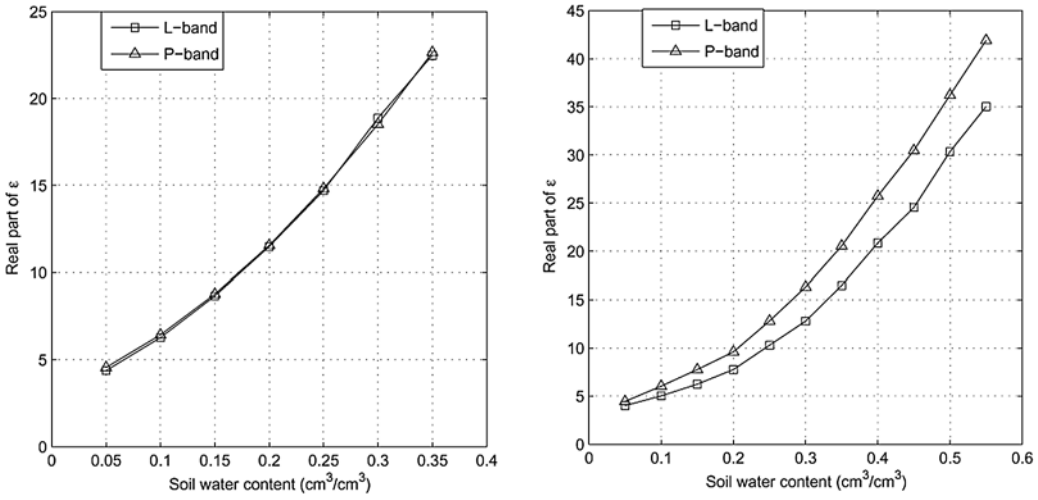

(a) Sand (b) Clay

Fig. 4 – Real part of dielectric constants of sandy and high clay content soils.

temperature-normalized width of the activation energy $\beta(W)$, the mean relation frequency $f_m(W)$, and the electric conductivity $\sigma(W)$ – are given in tables in [15].

Fig. 3 shows the calculated dielectric constants of a high clay content soils as a function of water content for L- and P- bands. We note that for P-band, the ionic conductivity term σ was included in the expression of ε''. Fig. 4 gives a comparison between the real part of dielectric constant ε' for the same soil type evaluated at L- and P- bands. At L-band, Fig. 5 shows that the calculated values of ε' for sandy soil were higher than those for the high clay content soil as much as ~ 6. On the other hand, a comparison of the calculated ε' at P-band showed that ε' for sandy soil was larger than that for high clay content soil by not more than ~ 2.5 at any given W.

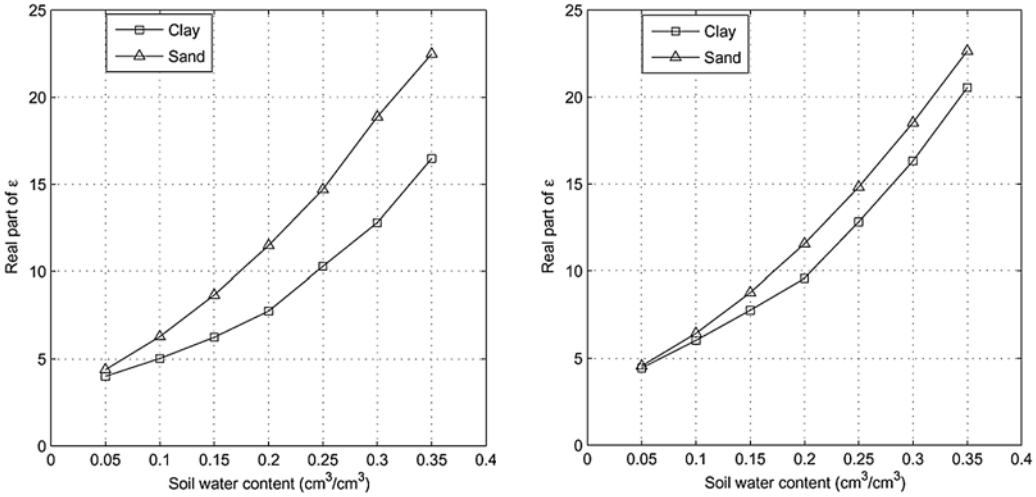

Fig. 5 – Real part of dielectric constants of sandy and high clay content soils.

4. SIMULATION RESULTS

The simulation of the losses due to the interface transmission shows the importance of the soil type on the attenuation of the incident wave. We have used the parameters of a full polarimetric facility named RAMSES (Radar Aéroporté Multi-spectrald'Etudes des Signatures) developed by French Aerospace Research Agency (ONERA). Table 1 describes the RAMSES system [21]. Table 2 gives the permittivity values corresponding to three different soils used in our simulations: dry, moist and wet soils.

On the three figures (Figs. 6, 7, and 8) appears a particular angle for which the losses due to the interface decrease much in vertical polarization (the Brewster

Table 1

Main characteristics of the RAMSES system

Band	Center Freq. [GHz]	Band width [MHz]	anten.	Polar.
P	0.43	75	Array	Full
L	1.3	200	Array	Full
S	3.2	300	Array	Full
C	5.3	300	Array	Full
X	9.5	1200	Both	Full
Ku	14.3	1200	Horn	Full

Table 2

Soil permittivities

Type of soil	dry	moist	wet
ε	3-j0.004	15-j0.24	30-j2.21

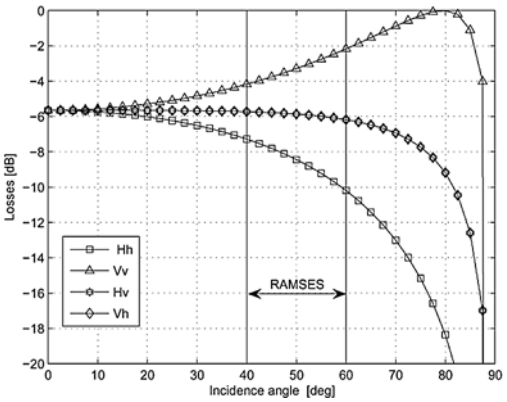

Fig. 6 – Interface losses for a wet soil.

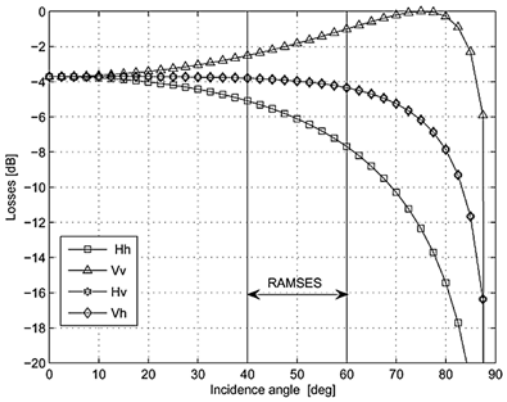

Fig. 7 – Interface losses for a moist soil.

angle). Another common point for the three soil types is that for the incidence angles used by the RAMSES radar (40°–60°), the attenuation due to the interface is less important in vertical polarization than in horizontal polarization. Then, in P-band, the detection of the buried objects are theoretically more easily exploitable in vertical polarization. On the other hand, more the soil is wet, more the attenuation due to the interface transmission is important. A priori, for a wet soil, the penetration is not very probable because the attenuation due only to the interface reaches 8 dB for the angles of interest. Moreover, for a dry soil, the incidence angle almost does not have an influence on the interface losses what lets predict a good penetration in the arid regions.

The losses due to the sub-surface penetration are also dependent on the soil type. For a dry soil, the incident wave thus reaches 17 meters of depth before being

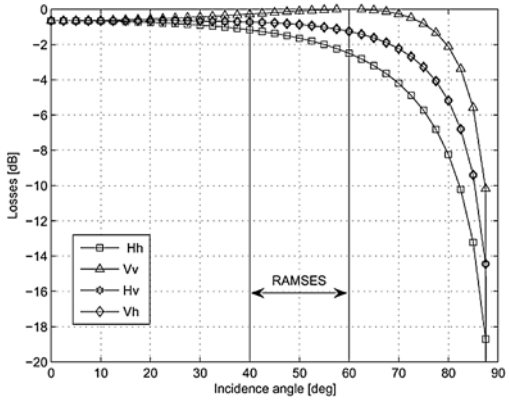

Fig. 8 – Interface losses for a dry soil.

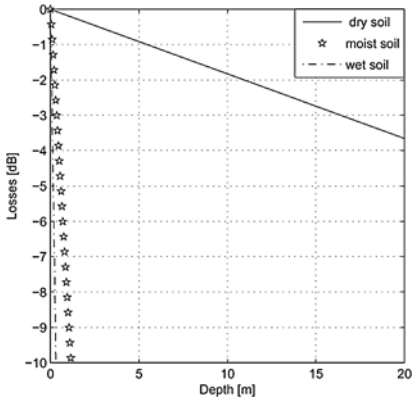

Fig. 9 – Sub-surface losses as function of depth.

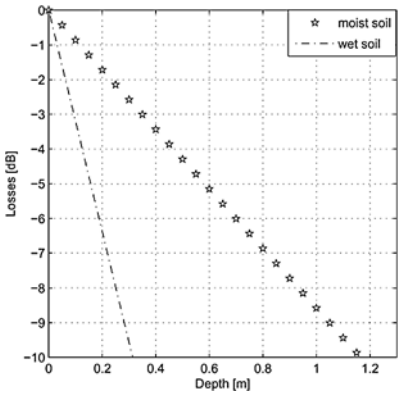

Fig. 10 – Sub-surface losses as function of depth.

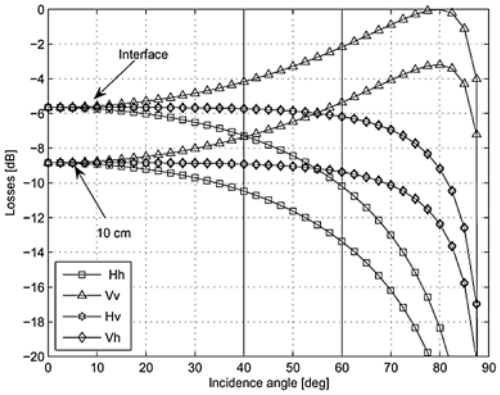

Fig. 11 – Total losses for a wet soil.

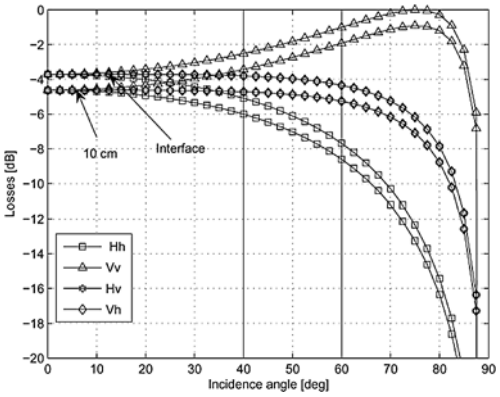

Fig. 12 – Total losses for a moist soil.

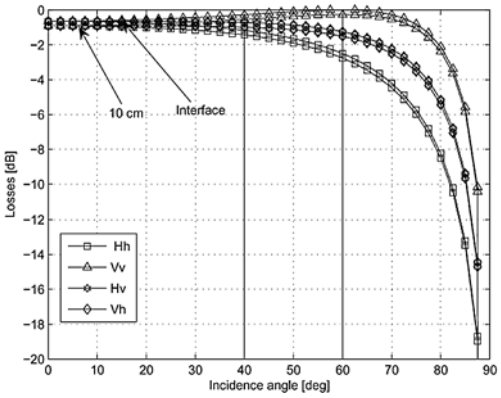

Fig. 13 – Total losses for a dry soil.

attenuated of 3 dB (Fig. 9). It is much stronger for wet soils: for a moist soil, after 30 cm the attenuation is higher than 3 dB and it is about 6 dB after 20 cm for a wet soil (Fig. 10).

The total losses due to the interface transmission and sub-surface penetration are shown in (Figs. 11, 12, 13).

- **Wet soil** (Fig. 11): for the incidence angles of interest, the total losses reach approximately 10 dB in horizontal polarization at 10 cm of the sub-surface. Thus, the penetration is not very probable in horizontal polarization as in cross-polarization in this type of soil.
- **Moist soil** (Fig. 12): the curves of the attenuation according to the incidence angle show that the penetration is still negligible in cross-polarization like in horizontal polarization (4 dB at the interface). In vertical polarization, the penetration reaches 10 cm with an acceptable attenuation.
- **Dry soil** (Fig. 13): in this case, the penetration is possible in all polarizations.

5. CONCLUSION

In this paper we have shown the penetration capabilities of low frequencies in the soil, especially the case of P-band (435 MHz). The simulation results show that the sounding of buried objects in arid and semi-arid environments is possible. This technique can be used in detection and identification of anti-personnel landmines at larger scales. Also, we have shown the importance of soil moisture in the interaction between the sub-surface and active mircowave systems. The dielectric constant of soil is highly dependent on soil moisture.

REFERENCES

1. F. T. Ulaby, R. K. Moore, A. K. Fung, *Microwave remote sensing: Active and passive*, **vol. I** (Norwood, MA: Artech House, 1981).
2. J. F. McCauley, G. G. Schaber, C. S. Breed, M. J. Grolier, C. V. Haynes, B. Issawi, C. Elachi, R. Blom, *Sub-surface valleys and geoarchaeology of the eastern Sahara revealed by Shuttle Radar*, Science, **218**, 1982, 1004–1020.
3. C. Elachi, L. E. Roth, G. G. Schaber, *Spaceborne radar sub-surface imaging in hyper arid regions*, IEEE Trans. Geosci. Remote Sensig, **GE-22**(4), 1984, 383–388.
4. G. G. Schaber, J. F. McCauley, C. S. Breed, G. R. Olhoeft, *Shuttle imaging radar: Physical controls on signal penetration and sub-surface scattering in the eastern Sahara*, IEEE Trans. Geosci. Remote Sensig, **GE-24**(4), 1986, 603–623.
5. M. G. Abdelsalam, R. J. Stern, *Mapping precambrian structures in the Sahara Desert with SIR-C/X-SAR radar: The neoproterozoic Keraf suture, NE Sudan*, J. Geophys. Research, **101**(E10), 1996, 23063–23076.

6. G. G. Schaber, J. F. McCauley, C. S. Breed, *The use of multifrequency and polarimetric SIR-C/X-SAR data in geologic studies of Bir Safsaf, Egypt*, Remote Sensing of Environment, **59**(2), 1997, 337–363.
7. T. G. Farr, C. Elachi, P. Hartl, K. Chowdhury, *Microwave penetration and attenuation in desert soil: A field experiment with the shuttle imaging radar*, IEEE Trans. Geosci. Remote Sensig, **GE-24**(4), 1986, 590–594.
8. C. Mätzler, *Microwave permittivity of dry sand*, IEEE Trans. Geosci. Remote Sensig, **36**(1), 1998, 317–319.
9. P. Paillou, G. Grandjean, N. N. Baghdadi, E. Heggy, T. August-Bernex, J. Achache, *Sub-surface imaging in south-central Egypt using low-frequency radar: Bir Safsaf revisited*, IEEE Trans. Geosci. Remote Sensig, **41**(7), 2003, 1672–1684.
10. K. K. Williams, R. Greely, *Radar attenuation by sand: Laboratory measurements of radar transmission*, IEEE Trans. Geosci. Remote Sensig, **39**(11), 2001, 2521–2526.
11. Y. Lasne, P. Paillou, T. August-Bernex, G. Ruffié, G. Grandjean, *A Phase signature for detecting wet sub-surface structures using polarimetric L-band SAR*, IEEE Trans. Geosci. Remote Sensig, **42**(8), 2004, 1683–1694.
12. G. Grandjean, P. Paillou, P. Dubois, T. August-Bernex, N. N. Baghdadi, J. Achache, *Sub-surface structures detection by combining L-band polarimetric SAR and GPR data: Example of the Pyla dune (France)*, IEEE Trans. Geosci. Remote Sensig, **39**(6), 2001, 1245–1258.
13. C. A. Balanis, *Advanced engineering electromagnetics* (New York: John Wiley and Sons Inc., 1989).
14. K. Zhang, D. Li, *Electromagnetic theory for microwaves and optoelectronics* (Berlin: Springer-Verlag, 1998).
15. J. R. Wang, *The dielectric properties of soil-mixtures at microwave frequencies*, Radio Sci., **15**(5), 1980, 977–985.
16. G. C. Topp, J. L. Davis, A. P. Annan, *Electromagnetic determination of soil water content: Measurements in coaxial transmission lines*, Water Resources Res., **16**(5), 1980, 574–582.
17. D. Wobschall, *A theory of the complex dielectric permittivity of soil containing water: The semidisperse model*, IEEE Trans. Geosci. Remote Sensig, **GE-35**(7), 1977, 49–58.
18. M. T. Hallikainen, F. T. Ulaby, M. C. Dobsen, M. A. El-Rayes, and L. K. Wu, *Microwave dielectric behavior of wet soil – Part I: Empirical models and experimental observations*, IEEE Trans. Geosci. Remote Sensig, **GE-23**(7), 1985,25–34.
19. F. T. Ulaby, R. K. Moore, A. K. Fung, *Microwave remote sensing: Active and passive*, vol. III (Norwood, MA: Artech House, 1986).
20. P. Dubois, J. van Zyl, T. Engman, *Measuring soil moisture with imaging radar*, IEEE Trans. Geosci. Remote Sensig, **33**(4), 1995, 915–926.
21. J.-M. Boutry, *ONERA airborne SAR facilities*, Proc. 2nd Int. Airborne Remote Sensing Conf., San Francisco, USA, 1996.